Accelerated biodegradation of iron-based implants via tantalum-implanted surface nanostructures

Min-Kyu Lee [a,b], Hyun Lee [c,d], Cheonil Park [a], In-Gu Kang [a], Jinyoung Kim [a], Hyoun-Ee Kim [a], Hyun-Do Jung [c,d,*], Tae-Sik Jang [e,**]

[a] Department of Materials Science and Engineering, Seoul National University, Seoul, 08826, Republic of Korea
[b] Querrey Simpson Institute for Bioelectronics, Northwestern University, Evanston, IL, 60208, USA
[c] Department of Biomedical-Chemical Engineering, Catholic University of Korea, Bucheon, 14662, Republic of Korea
[d] Department of Biotechnology, The Catholic University of Korea, Bucheon, 14662, Republic of Korea
[e] Department of Materials Science and Engineering, Chosun University, Gwangju, 61452, Republic of Korea

ABSTRACT

In recent years, pure iron (Fe) has attracted significant attention as a promising biodegradable orthopedic implant material due to its excellent mechanical and biological properties. However, in physiological conditions, Fe has an extremely slow degradation rate with localized and irregular degradation, which is problematic for practical applications. In this study, we developed a novel combination of a nanostructured surface topography and galvanic reaction to achieve uniform and accelerated degradation of an Fe implant. The target-ion induced plasma sputtering (TIPS) technique was applied on the Fe implant to introduce biologically compatible and electrochemically noble tantalum (Ta) onto its surface and develop surface nano-galvanic couples. Electro-chemical tests revealed that the uniformly distributed nano-galvanic corrosion cells of the TIPS-treated sample (nano Ta–Fe) led to relatively uniform and accelerated surface degradation compared to that of bare Fe. Furthermore, the mechanical properties of nano Ta–Fe remained almost constant during a long-term *in vitro* immersion test (~40 weeks). Biocompatibility was also assessed on surfaces of bare Fe and nano Ta–Fe using *in vitro* osteoblast responses through direct and indirect contact assays and an *in vivo* rabbit femur medullary cavity implantation model. The results revealed that nano Ta–Fe not only enhanced cell adhesion and spreading on its surface, but also exhibited no signs of cellular or tissue toxicity. These results demonstrate the immense potential of Ta-implanted surface nanostructures as an effective solution for the practical application of Fe-based ortho-pedic implants, ensuring long-term biosafety and clinical efficacy.

1. Introduction

In the past several decades, biodegradable metallic materials have served as one of the most promising strategies in regenerative medicine [1–4]. Biodegradable metals possess excellent mechanical properties, providing sufficient temporary support to resist the applied load, while the potential risk of long-term complications is effectively eliminated through the progressive degradation of the metals in the body [1,5–9]. Therefore, biodegradable metallic implants are best suited for the pur-poses of stabilizing fractured bone tissue and guiding bone healing. However, from a biological safety perspective, there are strict requirements for material selection, such as desirable degradation rates, balanced decline in mechanical properties with bone remodeling, and metabolism of the degradation byproducts in the body [5,10–12].

Fe is the most abundant metal in the human body and participates in a wide variety of metabolic processes, such as oxygen transport, energy metabolism, enzyme function, and DNA synthesis [11,13,14]. In particular, it is known for its vital role in bone homeostasis, and a deficiency of Fe causes bone disorders and impairs bone mineralization [15]. Previous studies have demonstrated that Fe possesses better me-chanical performance than most metals and exhibits no local or systemic toxicity in both short- and long-term *in vivo* studies [16,17]. However,

despite its immense potential for use in biodegradable orthopedic implants, the very low degradation rate of Fe in physiological media is the main obstacle to its successful clinical application [1,2,18]. Because long-lasting biodegradable materials in the body act like permanent materials, Fe implants inevitably provoke chronic foreign body reactions, causing implant loosening and eventual failure [1,19,20]. In addition, body fluids containing aggressive anions, such as chloride ions, can prompt localized preferential dissolution of Fe and lead to the formation of sharp, deep, and narrow pits on its surface that significantly deteriorate the mechanical performance and structural integrity of the Fe implant during its clinical service [3].

Practically, surface modification can provide a large pool of biocompatible material candidates and a high degree of freedom in designing the structure and optimizing the degradation rate of the Fe implant. Zhou et al. used a sandblasting process to develop a micro-roughened Fe surface that possessed a high specific surface area, ensuring physically accelerated degradation of Fe under body fluid conditions [21]. In a different study, Cheng et al. deposited micro-patterned gold disc films on the surface of Fe that generated micro-galvanic corrosion between Fe and gold under simulated body conditions and led to a significant increase in the Fe degradation rate [22]. Huang et al. revealed that small platinum surface patterns (up to 4 μm) were effective in accelerating the degradation rate of Fe via the formation of galvanic cells with the Fe matrix [23]. However, these micro-scale surface structures merely stimulated electrochemical reactions occurring on the Fe surface in a physiological environment without inducing any favorable bone tissue responses toward the implant surface due to their inert biological nature.

Over the past several decades, it has been demonstrated that nano-architectured surfaces influence a wide range of physical and biological phenomena due to their extremely large surface areas and size similarity to the extracellular matrix [24,25]. Most mammalian cells can specifically recognize nanoscale topographic features and directly respond by conforming their adhesion morphology to their surroundings and regulating their subsequent cellular behavior, such as survival, migration, proliferation, and differentiation [25,26]. However, despite these promising features, there has been no attempt to explore the capabilities of nanoarchitectured surfaces to modulate both the degradation rate and cellular responses of Fe implants. In this study, we propose a novel combination of a nanostructured surface and noble metal ion implantation as physical and electrochemical cues to achieve a high degradation rate and high bone tissue compatibility of the Fe implant. The recently developed target-ion induced plasma sputtering (TIPS) technique makes it possible to generate surface nanopatterns on metallic substrates via its massive ion bombardment and implantation capabilities [25,27]. With this technique, numerous target metal ions generated from the sputtering target gun are accelerated toward the substrate by applying an extremely high negative substrate bias voltage, which provides continuous implantation of target ions and non-uniform resputtering from the metal substrate. This unique feature enables the generation of distinct nanostructures on substrate surfaces and the incorporation of target metals into these surfaces [27].

In this study, to produce nano-galvanic cells over the surface of an Fe implant, we introduced tantalum (Ta) as a sputtering target, as it has a much higher corrosion potential (E_{corr}) than pure Fe and is known for its favorable interaction with bone tissue [24,28,29]. After TIPS treatment, we compared the surface morphology, microstructure, chemical composition, and electrochemical properties of the Fe implant (nano Ta–Fe) to those of an untreated Fe implant (bare Fe). We then compared the rates of corrosion and cellular behavior of the Fe implant before and after the TIPS treatment using an *in vitro* and *in vivo* rabbit femoral defect model.

2. Experimental methods

2.1. Sample preparation

Commercial bare Fe (99.8%, Hosung Industry, Korea) with a square shape (10 mm × 10 mm × 2 mm) was purchased for the surface characterization, electrochemical test, *in vitro* degradation, and cell viability test. All samples were cleaned by ultrasonification in ethanol 10 min before the tantalum (Ta) incorporation process. A Ta target (75-mm diameter, 5-mm thickness, 99.99% purity, Avention, Korea) was placed in a direct current (DC) magnetron sputtering gun (Ultech Co. Ltd, Daegu, Korea), and the vacuum chamber was sequentially pumped down to 5×10^{-4} Pa with rotary and diffusion pumps. To create a sufficient number of Ta ions, 50 W of target power was directly applied to the Ta target, and the working temperature and pressure were maintained at 0.6 Pa and 25 °C, respectively, during the process. A negative bias voltage (-1000 V) was supplied to the Fe substrate. In this paper, the Ta-implanted Fe is referred to as nano Ta–Fe.

2.2. Surface characterization

The surface morphology was observed using field-emission scanning electron microscopy (FE-SEM; JSM-6330 F, JEOL, Japan), and the compositional analysis of nano Ta–Fe was performed using high-resolution scanning transmission electron microscopy (STEM; JEM-2100 F, JEOL, Japan) conducted at 200 kV. The Ta distribution profile on the Fe surface was measured by the energy-dispersive X-ray spectroscopy (EDS) elemental spot analysis mode in STEM. The cross-sectional images and EDS mapping of the nano Ta–Fe surface after *in vitro* and *in vivo* degradation tests were obtained by focused ion beam (FIB) milling and FE-SEM equipped with EDS (FIB/FE-SEM; AURIGA, Carl Zeiss, Germany).

2.3. Electrochemical test

Electrochemical measurements were performed with a three-electrode system using a potentiostat/galvanostat (Model 273; EG&G Princeton Applied Research). A saturated calomel electrode (SCE) was utilized as the reference electrode, while a platinum coil served as the counter electrode. All samples were completely immersed in 1 L of simulated body fluid (SBF) solution adjusted to a pH of 7.4 at 37 ± 0.5 °C with an exposed area of 1 cm^2. The open circuit potential (OCP) was measured for 1 h. Electrochemical impedance spectroscopy (EIS) was performed from 100 kHz to 10 mHz at the OCP value, and potentiodynamic polarization curves were obtained ranging from an OCP value of ± 600 mV with respect to the saturated calomel electrode (SCE) at a scanning rate of 1 mV·s^{-1}. In addition, the surface voltage potential of the samples was measured by the scanning Kelvin probe (SKP) mode of an atomic force microscope (AFM; NX-10, Park systems, Korea). The scanning area was 25 μm × 25 μm, and the tests were performed at 25 °C in air.

2.4. In vitro static degradation tests

In vitro static degradation tests were performed at 37 °C in SBF solution for 1, 14, and 28 days (n = 3). After the immersion tests, all samples were gently rinsed with ethanol and ultrasonically cleaned for 1 h to prevent further degradation and observe the surface morphology of the corroded Fe substrates. The structural changes in the surface morphology as a function of the immersion period were investigated by FE-SEM equipped with an EDS attachment. The amount of Fe ion release in 25-ml SBF solution was recorded by performing inductively coupled plasma atomic emission spectrometry (ICP-AES) after the static immersion test.

2.5. In vitro degradation and mechanical property evaluation

An *in vitro* degradation test was performed to evaluate the changes in the mechanical properties as a function of the degradation time. The mechanical stability after degradation was assessed over an immersion period of 12 and 40 weeks. Dog bone samples with a thickness of 450 µm were used for the degradation and mechanical test in accordance with American Society for Testing and Materials (ASTM) E8/E8M − 08. All samples were immersed in SBF solution, and the temperature was maintained at 37 °C. To create an environment for accelerated degradation, the SBF was replaced every 2 days for 40 weeks. After 12 and 40 weeks of immersion, all samples were extracted from the SBF solution and ultrasonically cleaned with ethanol to prevent further degradation. The surface roughness of the samples was examined by laser scanning microscopy (OLS 4100, Olympus, Japan). For the tensile test, a universal testing machine (Instron 5580, Instron Corp., Canton, MA) was used with a fixed loading rate of 1 mm/min, and the thickness loss of samples was measured by a vernier calipers at three different regions (upper, middle, and lower) of each sample after specific time interval of degradation test.

2.6. In vitro cellular assays

The *in vitro* cytocompatibility of bare and nano Ta–Fe was assessed in terms of cell attachment and proliferation with osteoblast cells (MC3T3, ATCC, CRL-2593). Incubated cells were seeded onto the bare Fe and nano Ta–Fe surfaces at a density of 2×10^4 cells/mL for the cell attachment and cell proliferation assays. Osteoblast cells were cultivated in a cell incubator containing 5% CO_2 at 37 °C. A culturing medium (α-MEM, Welgene Co., Ltd., Korea) with 10-mM β-glycerophosphate (Sigma), 10-µg mL−1 ascorbic acid, 1% penicillin-streptomycin, and 10% fetal bovine serum (FBS) was used.

A cell attachment test of bare and nano Ta–Fe samples was performed using fluorescence imaging for 1 and 3 days. All samples were disinfected with absolute ethanol under ultraviolet irradiation overnight prior to cell seeding. Live cell staining was performed by calcein acetoxymethyl ester (Calcein AM, Invitrogen, USA) for 40 min of incubation. After 1 and 3 days of culturing, the morphology of the attached cells was observed by confocal laser scanning microscopy (CLSM; C1 PLUS, Nikon, Tokyo, Japan).

Cell proliferation was assessed using the MTS assay (MTS, Promega, Madison, WI, USA) for 1 and 3 days. An extraction medium of bare and nano Ta–Fe was used after 2 days of immersion in Dulbecco's modified Eagle's medium (DMEM; Gibco, Germany). The extraction medium (0.5 mL) was placed in a 24-well plate with 0.5 mL of DMEM. The control groups were as follows: DMEM containing 10% FBS, and DMEM containing 10% dimethyl sulfoxide (DMSO) as a positive and negative control, respectively [30]. The total cell seeding density of the samples was 2×10^4 cells/mL. The amount of formazan product was assessed after 1 and 3 days of culturing with the absorbance at 490 nm using a microplate reader.

2.7. In vivo degradation test

2.7.1. In vivo animal model and surgical procedure

All *in vivo* procedures involving animal selection, surgical protocol, management, and sacrificial procedures were authorized by the Ethics Committee on Animal Experimentation of the Institutional Animal Care and Use Committee of GENOSS (GEN-IACUC, no. 1902–01). The *in vivo* experiment was conducted using a bone marrow cavity model in 12-week-old male New Zealand white rabbits (male, body weight 2.5–3.0 kg, DBL Inc., Korea) as described in previous research [31,32]. Six rabbits were used in this animal experiment, and one specimen was placed on both sides of the bone marrow cavity for each rabbit. For micro-CT and histological analysis, three specimens per each group were used (n = 3). The micro-CT and histological analysis were performed

The rabbits were anesthetized by intramuscular injection with an anesthetic mixture of xylazine (1.5 mL, Rompun 2%, Bayer Korea, Korea), tiletamine (0.5 mL, Zoletil, Virbac Lab, France), and a local anesthetic, lidocaine (0.5 mL with 1:100,000 epinephrine, Yuhan Corporation, Korea). A round hole (2-mm diameter) was created in the patellar groove using a hand drill, and bare and nano Ta–Fe pins (2 mm in diameter and 10 mm in height) were individually inserted in the bone marrow cavity in the femur of each rabbit. The wounds were closed with sutures. A postoperative antibiotic, 0.3 mL of gentamicin (Samu Median, Korea) in saline solution, was carefully injected for 3 days. The rabbits were sacrificed after 1 and 4 months of implantation.

2.7.2. Micro-computed tomography (micro-CT) analysis and morphological evaluation

After sacrificing the animal, to measure the inserted pin position, the femur bone tissues were visualized by micro-CT (Skyscan 1173, Skyscan, Kontich, Belgium) under specific conditions (voltage of 130 kV, resolution of 6 µm, and current of 60 µA). Post-processing software (NRecon and Data Viewer 1.4, Skyscan, USA) was used to reconstruct three-dimensional (3D) and two-dimensional (2D) images of the samples.

The Fe pins embedded in resin blocks were cut to make cross-sections, and cross-sectional pin surfaces were polished with 1000, 2000, and 4000 grit SiC paper. The polished cross-section of Fe pins was coated with platinum for further SEM and EDS observation (FE-SEM; JSM-6330 F, JEOL, Japan). The cross-sectional morphology of each pin was observed using FE-SEM and EDS mapping at four different regions (top, bottom, left, and right) of each sample after 4 and 16 weeks of *in vivo* degradation testing.

2.7.3. Histological evaluation

The samples for histological evaluation were divided into two parts. One part was fixed in 10% formaldehyde solution and immersed in resin (Technovit 7200) for hematoxylin–eosin (H&E) staining. The other part of the harvested bone was embedded in paraffin for Prussian blue and immunohistochemistry with primary anti-CD68 staining (CD68, abcam, USA). The slide of the blocks (thickness < 5 µm) was fabricated by cutting and grinding. The number of macrophages was calculated in the unit area of the image field. A panoramic digital slide scanner (Panoramic 250 Flash III, 3DHISTECH Ltd., Hungary) was used to observe microscopic images of the stained sections.

2.8. Statistical analysis

All experiments were conducted with three samples per group. Statistical analysis was performed by the Statistical Package for the Social Sciences (SPSS 23, SPSS Inc., USA) software, and all experimental data were converted to mean ± standard deviation. The normality of the variables was assessed using the Shapiro−Wilk test, and the statistical analysis was performed by one-way analysis of variance followed by Tukey's post-hoc comparison. A *p*-value of <0.05 was deemed significant.

3. Results

3.1. Surface characterization

The surface and cross-sectional morphology of the Fe substrate before and after TIPS treatment was investigated with FE-SEM, FIB, and STEM. TIPS treatment led to an obvious change in the surface features of the Fe substrate (Figs. 1 and S1). Specifically, the smooth surface morphology of bare Fe with several polishing marks completely disappeared after the treatment, and homogeneous nanostructures were created over the Fe surface (Fig. 1(a)–(d)). The low-magnification image reveals that the Fe substrate continued to possess macro- and micro-scale surface flatness after the TIPS treatment; however, the high-magnification and cross-sectional images reveal that well-organized
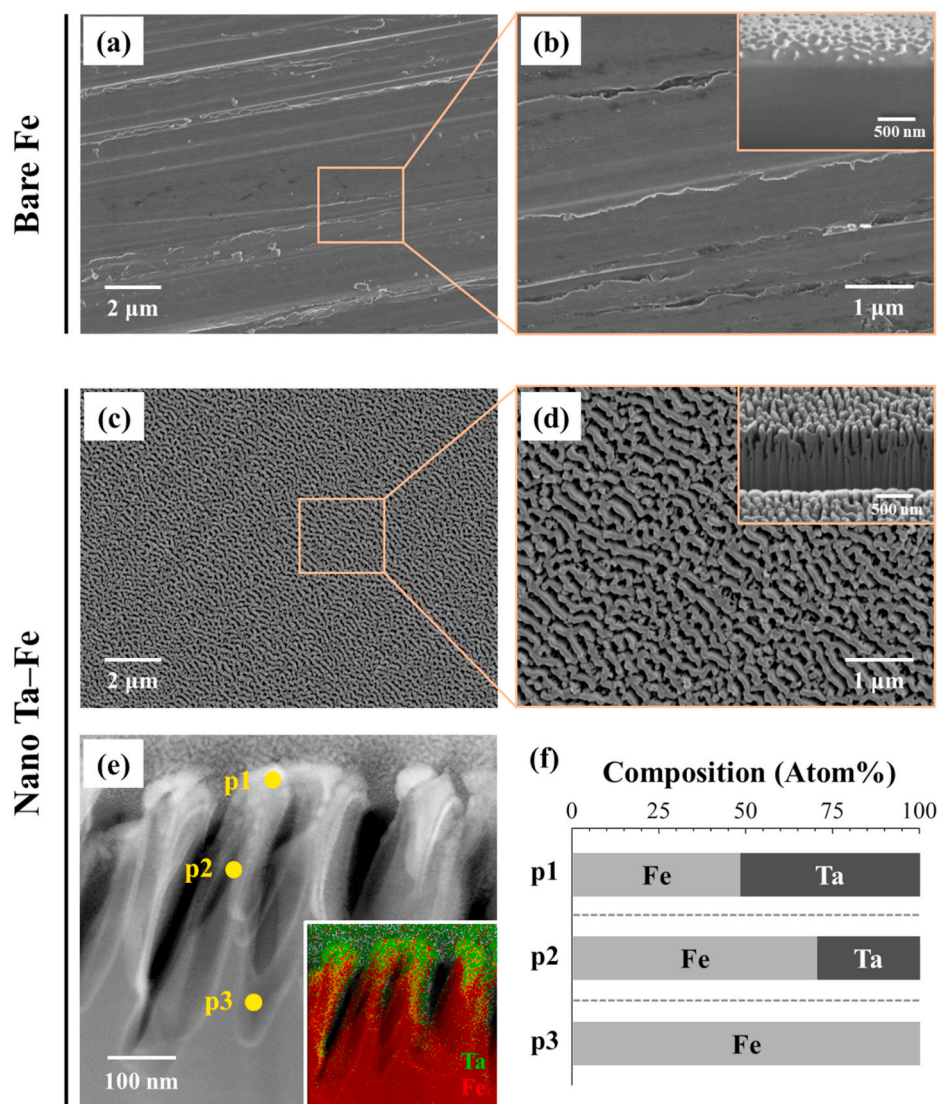
Fig. 1. Representative surface field-emission scanning electron microscopy (FE-SEM) images of (a), (b) bare Fe and (c), (d) nano Ta–Fe at high and low magnification. The insets in (b), (d) display the cross-sectional focused ion beam (FIB)/FE-SEM image of the surface of bare Fe and nano Ta–Fe. (e) Cross-sectional scanning transmission electron microscopy image of nano Ta–Fe with energy-dispersive X-ray spectroscopy mapping (inset), and (f) chemical compositions at three regions in e (p1: top, p2: middle, and p3: bottom).

nanoridges were strongly adhered to the Fe substrate with an average height, width, and gap of 345 ± 18 nm, 200 ± 18 nm, and 102 ± 10 nm, respectively. There was no sign of a physical interface between the surface nanostructure and substrate. The STEM and EDS mapping images clearly display the cross-sectional elemental distributions for the major elements, Ta and Fe, after the TIPS treatment. The implanted Ta was mostly distributed at the top region of the nanoridges, whereas the bottom region appeared to be composed of bare Fe without Ta (Fig. 1e). From the EDS analysis at three different locations in Fig. 1(e) (p1: top, p2: middle, and p3: bottom), the highest atomic concentration of Ta appeared to be only ~50 at% at the top of the nanoridge surface, which gradually decreased toward the bottom of the nanoridges to 0 at% (Table S1). According to the supplemental XPS analysis (Fig. S2), the metallic Ta peaks (Ta 4f, Ta 4d, and Ta 4p) were clearly detected from the surface of Fe substrate after the TIPS treatment with typical Ta chemical state of Ta_2O_5 in high-resolution spectrum of Ta 4f. Based on its morphology and elemental composition, the Fe substrate after TIPS treatment is referred to as nano Ta–Fe, while the untreated Fe is referred to as bare Fe (Fig. 1(f)).

3.2. Degradation properties of bare Fe and nano Ta–Fe

3.2.1. Electrochemical behavior

The electrochemical behavior of bare Fe and nano Ta–Fe was investigated using SKP potentiometry, potentiodynamic polarization, and EIS analysis (Fig. 2), and the electrochemical parameters calculated by Tafel extrapolation from potentiodynamic polarization curves are provided in Table S2. Fig. 2(a) presents a map of the surface potential distribution obtained by SKP measurement from the bare Fe and nano Ta–Fe samples. A nearly uniform distribution of surface potential was observed for both samples; however, the development of a nanoridge surface with Ta implantation led to a decrease in the average surface potential from −491 mV to −573 mV. This trend was also observed in the results of potentiodynamic polarization analysis (Fig. 2(c) and Table S2). The anodic region of the polarization curve (above E_{corr}) was related to the dissolution of Fe in the SBF solution, while the cathodic region (below E_{corr}) was related to the cathodic evolution of hydrogen gas. After TIPS treatment, E_{corr} of nano Ta–Fe shifted toward more negative (active) potential values by −26 mV, while the corrosion current density (I_{corr}) increased from 4.92 to 13.84 μA cm^{-2}. The degradation rate of Fe appeared to be accelerated by the development of a nanoridge surface with Ta implantation, and the average degradation rate (mm·year^{-1}) was 281.3% higher for nano Ta–Fe than bare Fe (Table S2).

Fig. 2(d) presents the results of EIS analysis in the Nyquist representation. In the Nyquist plots, both the bare Fe and nano Ta–Fe samples exhibit a semicircle in the high-to-medium frequency region, followed by a straight line with a 45° phase angle in the low-frequency region. In
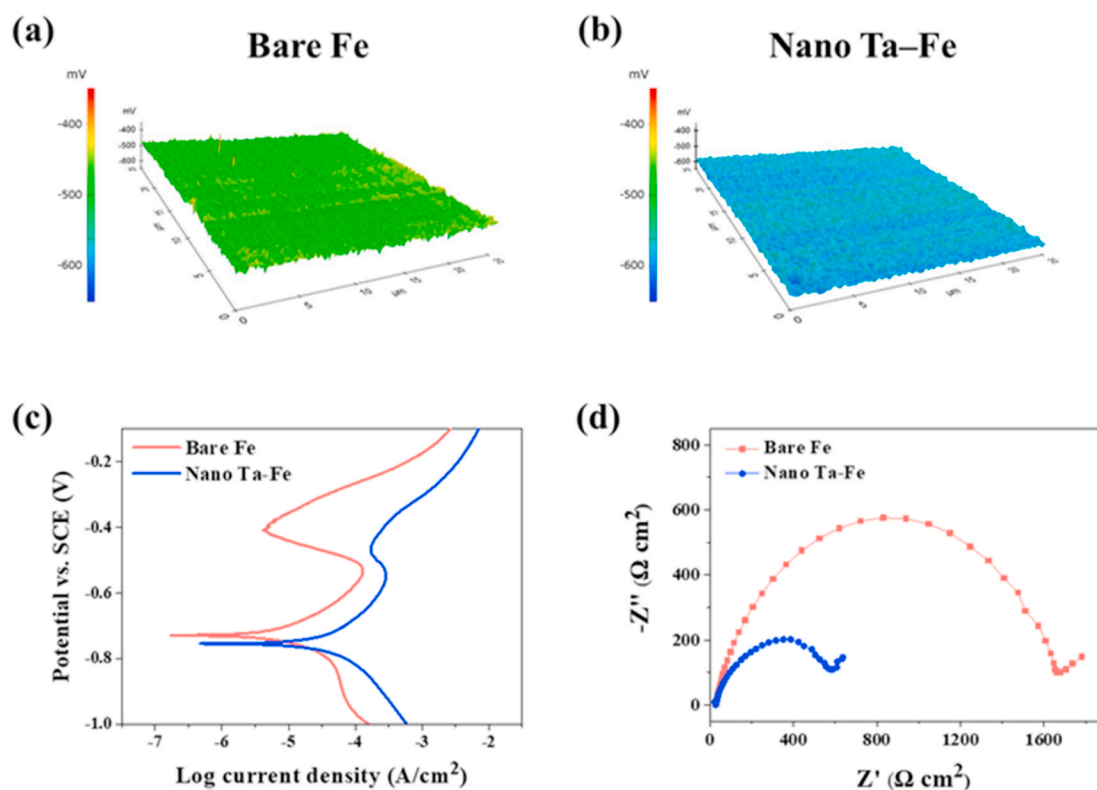
Fig. 2. Electrochemical corrosion behaviors: Scanning Kelvin Probe maps of (a) bare Fe, (b) nano Ta–Fe, (c) Potentiodynamic polarization curves, and (d) Nyquist plots.

general, the semicircular portion of a Nyquist plot directly corresponds to an electron transfer limited process at the metal surface/solution interface, and its diameter represents the electron transfer resistance of the corrosion process. By comparing the Nyquist plots of bare Fe and nano Ta–Fe, it is clear that the electron transfer resistance was substantially reduced after the TIPS treatment, which indicates that the nanoridge surface with Ta implantation effectively accelerated the corrosion rate of the Fe substrate.

3.2.2. Degradation behavior with static immersion test

To investigate the *in vitro* degradation behavior of bare Fe and nano Ta–Fe, both samples were immersed in SBF solution, and their surface morphology, concentration of Fe ion release, and degradation thickness on day 1, 14, and 28 of immersion are presented in Fig. 3. For bare Fe, there was no substantial change in the surface morphology for 28 days of immersion; most of the surface appeared flat, smooth, and clear throughout the testing period, while tiny degradation pits appeared on day 14, and several of them grew quickly, forming broad and deep craters on the surface on day 28. In contrast, nano Ta–Fe underwent dramatic morphological changes during the immersion test. On day 1 of immersion, surface degradation features appearing as small specks were formed on the surface of nano Ta–Fe, whose appearance became increasingly rough and irregular with increasing immersion time. After 28 days of immersion, the surface of nano Ta–Fe was uniformly roughened without any sign of severe local degradation. High-magnification surface and cross-sectional images revealed that these roughened surface features were due to the formation and propagation of cracks on the nanostructured surface layer of nano Ta–Fe.

Up to day 1 of immersion, nano Ta–Fe retained its distinct nano-roughened surface features, and there were no visible morphological changes. However, after 14 days of immersion, the nanostructured surface layer was cracked, and a narrow cross-sectional gap of submicron size appeared between the nanostructured surface layer and the Fe substrate as a result of preferential degradation of the Fe substrate. With

continuous immersion, the surface cracks were propagated and broadened, leaving the underlying Fe substrate partially visible on day 28 of immersion. Although large cracks were formed on the surface of nano Ta–Fe, the nanostructured surface was not fully delaminated and preserved close contact with the Fe substrate in the cross-sectional observation. In addition, it should be noted that there were no deep or narrow degradation pits on the Fe surface regardless of the immersion time and degree of degradation.

To investigate the *in vitro* degradation rate of the samples, we measured the thickness of the degradation byproducts, the degradation depth of the Fe substrate, and the number of released Fe ions from the bare Fe and nano Ta–Fe samples up to 28 days for the SBF immersion condition. As illustrated in Fig. 3(B)–(D) and S3, the degradation rate of Fe was significantly increased by the development of the nanostructured surface layer with Ta implantation. Although bare Fe had large variations in the maximum and minimum thickness of the degradation byproducts and average degradation depth of the Fe substrate due to its localized surface degradation behavior, nano Ta–Fe displayed higher values for both the thickness of the degradation byproducts and the depth of the Fe substrate degradation, and narrower value ranges than those of bare Fe for the entire measurement period (Fig. 3(B) and (C)). This tendency was also observed in the result of the Fe ion release test (Fig. 3(D)). Bare Fe slowly released Fe ions with increasing immersion time, reaching an ion concentration of 22.4 µg/ml on day 28 of immersion. In contrast, nano Ta–Fe demonstrated a significantly increased degradation rate compared with bare Fe. Specifically, Fe ions were released from the surface of nano Ta–Fe much more rapidly, resulting in a twofold higher concentration of Fe ions for the overall immersion time. The concentration of Fe ions on day 28 of immersion was 51.0 µg/ml, which was 228% higher than that of bare Fe. From the supplemental Ta ion release result (Fig. S4), there was no release of Ta ions from the surface of nano Ta–Fe sample during the entire 28-day observation period.
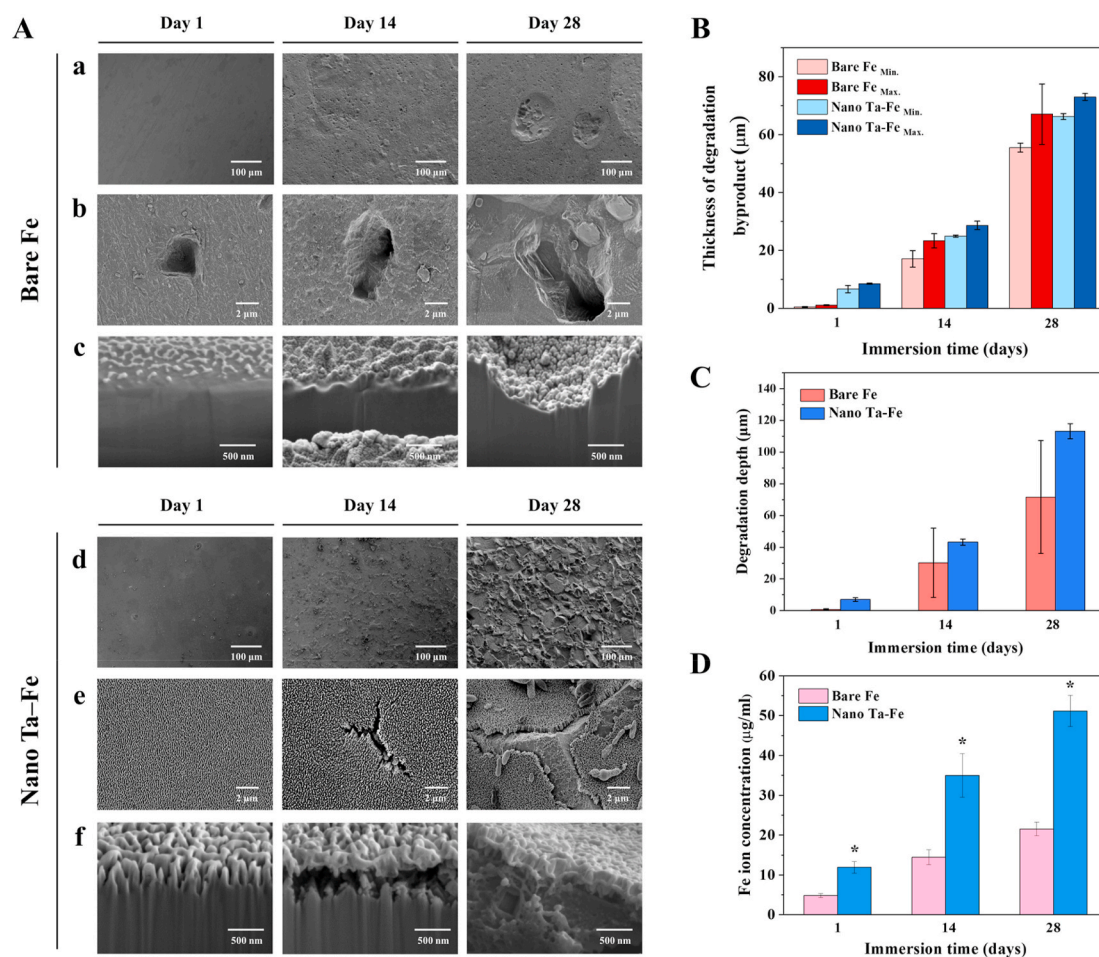
Fig. 3. *In vitro* degradation test for 28 days in simulated body fluid solution to observe the degradation pit formation and degradation rate. (A) Field-emission scanning electron microscopy (FE-SEM) images of surface morphology of bare Fe and nano Ta–Fe at (a), (d) low magnification and (b), (e) high magnification, and (c), (f) cross-sectional focused ion beam (FIB)/FE-SEM images. (B) Thickness of degradation byproducts (abbreviations Min. and Max. Denote the minimum and maximum thickness, respectively, of the degradation byproducts). (C) Degradation depth of bare Fe and nano Ta–Fe. (D) Released Fe ion concentration of bare Fe and nano Ta–Fe.

3.3. Mechanical properties of bare Fe and nano Ta–Fe

Mechanical properties are some of the most important factors of load-bearing biodegradable implants. In particular, to provide mechanically safe and reliable support to damaged bone tissue, implants should have sufficient strength, structural rigidity, and flexibility during the bone healing period. Therefore, the long-term mechanical durability of bare Fe and nano Ta–Fe was tested for the SBF immersion condition for up to 40 weeks. Fig. 4(A) presents optical images of the mechanical test samples before and after immersion at week 12 and 40. Localized degradation regions were observed on the surface of bare Fe with different contrast as light gray dots at week 12 of immersion. With increasing immersion time, its surface became markedly rough, and deep craters were randomly distributed on the surface. In contrast, nano Ta–Fe appeared relatively uniform in color and texture over its entire surface, and no significant change or abnormality in appearance was observed with time. In contrast, as indicated in Fig. 4(B)–a, the results of the thickness loss demonstrated progressive and rapid degradation of nano Ta–Fe despite it exhibiting fewer morphological changes than bare Fe. During the entire immersion period, nano Ta–Fe exhibited higher levels of thickness loss than bare Fe, and the difference between them became more pronounced with increasing immersion time.

The mechanical behavior of the bare Fe and nano Ta–Fe samples was evaluated by tensile tests before and after immersion for 12 and 40 weeks. Typical tensile stress–strain curves of each sample are presented

in Fig. 4(B)–b. All curves exhibited a steep initial linear slope in the elastic region and a gradual increase in the stress with deformation in the plastic region, followed by ductile failure after reaching the ultimate tensile strength (UTS). Although the bare Fe and nano Ta–Fe samples had almost identical curve shapes before the immersion test, only bare Fe exhibited a substantial loss of mechanical properties as the immersion time increased. As illustrated in Fig. 4(B)–c and (B)-d, the UTS and elongation rate of bare Fe gradually decreased with immersion time, experiencing a 32% and 25% reduction, respectively, at week 40 than before immersion, while nano Ta–Fe had almost the same values with no statistical difference. The difference in the UTS and elongation rate between the bare Fe and nano Ta–Fe samples became more pronounced with immersion time.

Because localized surface degradation has a large effect on the rapid deterioration of the mechanical properties of an implant, gradual changes in the surface morphology with immersion time are also represented by 3D images in Fig. 4(C), and the detailed surface roughness values (R_a: arithmetic mean deviation, R_q: root mean square deviation, R_p: maximum profile peak height, and R_v: maximum profile valley height) are presented in Fig. S5. For bare Fe, there were substantial changes in the surface morphology up to 40 weeks of immersion. Specifically, the flat and smooth surface of bare Fe became completely rough and irregular with deep and wide dimples distributed all over the surface at week 12, which became more prominent at week 40. In contrast, the surface of nano Ta–Fe appeared more uniformly corroded
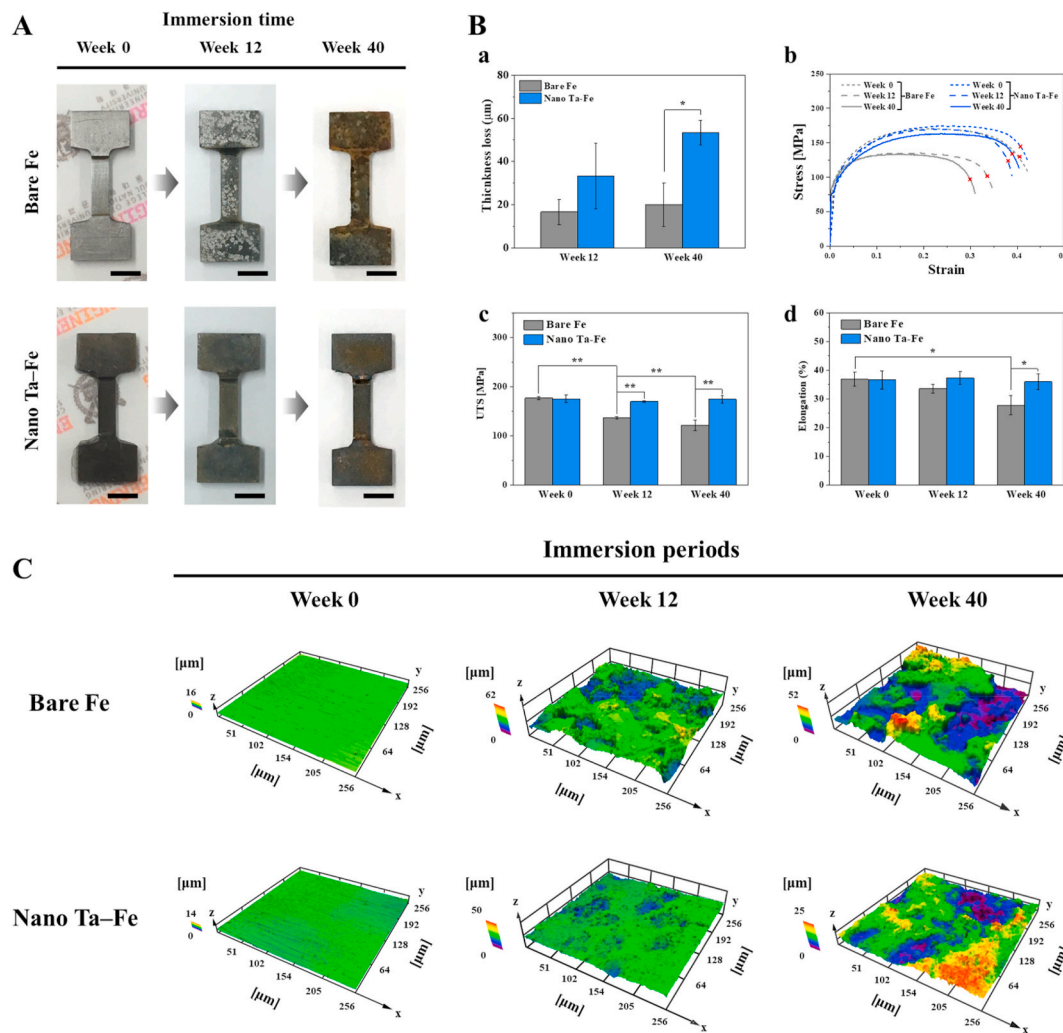
Fig. 4. (A) Optical images of bare Fe and nano Ta–Fe before and after 12 and 40 weeks of immersion in simulated body fluid solution. The inset scale bar is 500 μm. (B) Tensile tests of bare Fe and nano Ta–Fe up to 40 weeks of immersion; (a) thickness loss, (b) stress–strain curves, (c) ultimate tensile strength, and (d) elongation rate (*: $p < 0.05$ and **: $p < 0.005$). The symbols x indicate the break points. (C) Three-dimensional surface topography as a function of immersion period using a laser scanning microscope.

and nearly flat up to 12 weeks of immersion. Although nano Ta–Fe also displayed a micro-scale roughened surface at week 40, only shallow craters were sparsely distributed, and its average surface roughness (R_a and R_q) and maximum peak (R_p) and valley heights (R_v) were almost three times lower than those of bare Fe.
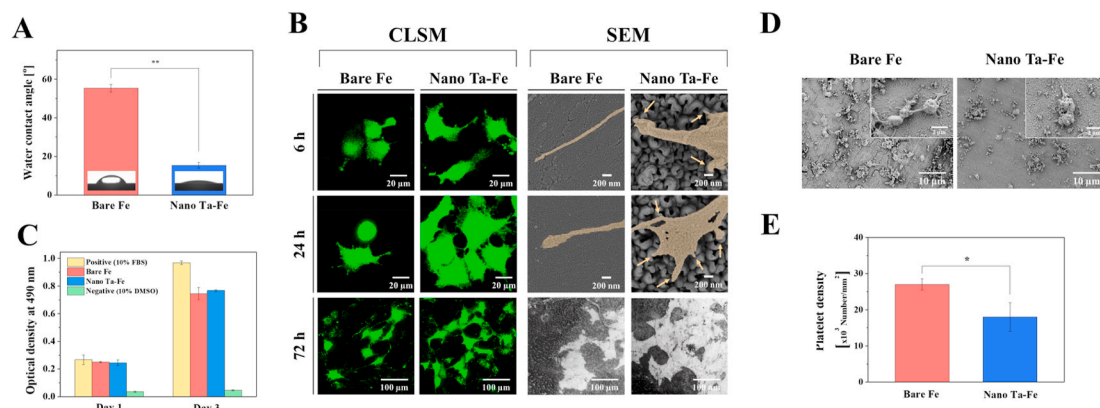

Fig. 5. (A) Water contact angles of bare Fe and nano Ta–Fe. (B) Low-magnification confocal laser scanning microscopy and high-magnification field-emission scanning electron microscopy (FE-SEM) images of attached osteoblast cells (MC3T3) on bare Fe and nano Ta–Fe surfaces after culturing for 6, 24, and 72 h. (C) The relative value of viable osteoblast cells growing in extracted culturing media with bare Fe and nano Ta–Fe immersions. (D) Representative FE-SEM images of adhered platelets on the surface of bare Fe and nano Ta–Fe. (E) Adhered platelet density on the bare Fe and nano Ta–Fe surface. (*: $p < 0.05$ and **: $p < 0.005$).

3.4. Wettability and in vitro cellular response

Wettability is one of the most important surface properties of an orthopedic implant affecting cell–implant interaction and bone tissue response. Therefore, prior to investigating the cellular responses, the water contact angle formed on the bare Fe and nano Ta–Fe samples was measured (Fig. 5(A)). Compared to bare Fe, nano Ta–Fe exhibited substantially enhanced surface hydrophilicity, as illustrated in Fig. 5(A). The angle of the water droplet was spread out on the nano Ta–Fe surface with a contact angle of 15°, while bare Fe displayed a near hydrophobic surface (contact angle ≈ 55°).

For the *in vitro* biocompatibility evaluation of bare Fe and nano Ta–Fe, the response of osteoblasts (MC3T3) to both samples was closely examined in terms of cell adhesion morphology and viability. Fig. 5(B) presents CLSM and FE-SEM images of the samples after 6, 24, and 72 h of culturing, which indicate that the cells had a more pronounced morphological response to the surface of nano Ta–Fe than to bare Fe at all time points. On the surface of nano Ta–Fe, cells were tightly adherent and spread extensively, causing closer cell–cell interactions and better cell surface coverage than bare Fe only after 24 h of incubation. In addition, a larger number of filopodia-like cell protrusions were produced at the spreading edge of the cells on nano Ta–Fe compared to bare Fe. Multiple small protrusive structures (indicated by arrows) extended from the cell and anchor to the top of the surface nanostructures, leading to a proper extension of cell surfaces, whereas the cells on bare Fe formed a single needle-like (long and narrow) cell protrusion. After 72 h of culturing, although both samples had a substantial amount of degradation byproducts covering a large portion of the cell surface, the cells preserved their integrity and viability without a noticeable change in the adhesion shape or detachment from both surfaces. In addition, the supplemental *in vitro* experiments confirm that even after 72 h pre-degradation in SBF solution, the nano Ta–Fe sample showed larger number of cells and better cell spreading appearance than the bare Fe (Fig. S6).

To further investigate the effect of the degradation byproducts, especially ionic products (Fe^{2+} and Fe^{3+}), on osteoblast viability, the cells were cultured for up to 3 days in the culturing media obtained after 2 days of incubation with bare Fe and nano Ta–Fe samples (Fig. 5(C)). For reference, culturing media containing 10% FBS or 10% DMSO were also included in this measurement as a positive and negative control, respectively. After 1 day of culturing, the bare Fe and nano Ta–Fe samples exhibited no sign of cytotoxicity to osteoblasts; their cell viability levels were almost identical to the positive control without any statistical significance (vs. bare Fe: $p = 0.741$, and vs. nano Ta–Fe: $p = 0.552$). Although the bare Fe and nano Ta–Fe samples demonstrated somewhat lower levels of cell viability than the positive control after 3 days of culturing, the cells in the culturing media obtained with bare Fe and nano Ta–Fe samples also significantly proliferated (with an almost threefold increase) between days 1 and 3, whereas the negative control exhibited a negligible level of cell viability at all time points.

The blood compatibility of bare Fe and nano Ta–Fe was also confirmed by the results obtained from the material-induced platelet adhesion and aggregation test, which is regarded as an important factor influencing the outcome of a medical implant and its success. After incubating the samples into a platelet-rich plasma solution for 45 min, the adhered platelet morphology and density on the surface of bare Fe and nano Ta–Fe are presented in Fig. 5(D) and (E). In the low-magnification FE-SEM image, a large number of platelets adhered to and locally aggregated on the surface of bare Fe, and their morphology was noticeably changed into irregular central bodies with multiple long dendritic pseudopodia at the adhesive points in the high-magnification image. In contrast, the number of adhered platelets on the nano Ta–Fe surface was apparently reduced, and the platelets retained their original spherical shape with nearly no formation of pseudopods. As illustrated in Fig. 5(E), nano Ta–Fe exhibited a 34% lower density of adhered platelets than bare Fe with statistical significance ($p < 0.05$).

3.5. In vivo degradation analysis

To evaluate the *in vivo* degradation rate of the materials, cylindrically shaped bare Fe and nano Ta–Fe implants were inserted into each side of the femoral bone marrow cavity of a rabbit, and after 4 and 16 weeks, 3D volumetric and 2D cross-sectional surface morphometric analysis was performed by micro-CT and FE-SEM/EDS. As illustrated in Fig. 6(A), in the 3D images of the inserted implants with bone tissue and the 2D coronal and transverse images (without bone tissue), both implants appeared to have a uniform and regular surface morphology with no macroscopic deformation or damage over large surface areas up to week 16 after implantation. In addition, there was no indication of bone erosion or resorption around either implant during the observation period. The quantitative residual volume of the implants was measured by micro-CT before and after implantation at weeks 4 and 16 (Fig. 6(B)). For the *in vivo* case, the nano Ta–Fe implant lost its volume at a faster rate than bare Fe, exhibiting a 211.0% faster average volumetric loss value than that of bare Fe from the initial volume to week 16.

In addition, the high-magnification FE-SEM images indicated the localized biodegradation of the bare Fe implant. Specifically, a narrow and deep pit was formed on the surface of bare Fe at week 4, and it was further broadened with an increased implantation period (blue rectangle regions in Fig. 6(C)). Although the nano Ta–Fe implant also exhibited a roughened surface topography, only small-scale roughness features appeared without any deep or localized pitting on its surface during the entire implantation period. In the EDS mapping results, the thin and uniform distribution of oxygen (a possible degradation product from the Fe substrate) was clearly observed on the surface of nano Ta–Fe, whereas it was locally and significantly accumulated only near the surface pit or deep crater on the surface of bare Fe.

3.6. In vivo histological and immunohistochemical analysis

Histological and immunohistochemical images of the bare Fe and nano Ta–Fe implants after implantation at weeks 4 and 16 are presented in Fig. 7(A)–(C). The transverse sectioned implants were stained with H&E and Prussian blue, and the expression of macrophages was detected through CD68 immunostaining. As illustrated in Fig. 7(A), the bare Fe implant exhibited non-uniform surface degradation. After 4 weeks of implantation, the surface of bare Fe in the blue rectangle region became rough, and degradation byproducts surrounded its surface, displaying a brownish color in the high-magnification H&E image, whereas there were no noticeable morphological changes in the red rectangle region. As the implantation period progressed, bare Fe continued to exhibit a rough and irregular surface morphology, and a significant number of degradation byproducts were generated only in the blue rectangle region. In contrast, for the nano Ta–Fe implant, a uniform surface morphological change was observed with increased implantation time. In both the blue and red rectangle regions, nano Ta–Fe appeared to retain a smooth surface morphology after 4 weeks of implantation, and it was not noticeably changed when the implantation further progressed to week 16.

The presence of Fe ions in the surrounding bone marrow tissue was confirmed by Prussian blue staining, in which ferric ions (Fe^{3+}), an oxidized form of the Fe degradation byproduct, in the tissue appeared to be blue, as illustrated in Fig. 7(B). After 4 weeks of implantation, the bare Fe implant exhibited only negligible Fe^{3+} ion penetration into the surrounding tissue. In low- and high-magnification images, almost all tissues were stained red, and it was difficult to identify the specific penetration depth of Fe^{3+} ions into the bone marrow tissue. For the nano Ta–Fe implant, its low-magnification stained image appeared to be similar to that of bare Fe at week 4 of implantation. However, in the high-magnification image, a light-blue stained region was clearly observed, and its thickness appeared relatively constant with an average thickness of 56.8 ± 6.3 μm. As the implantation period increased, the nano Ta–Fe sample displayed more pronounced and widespread Fe^{3+}
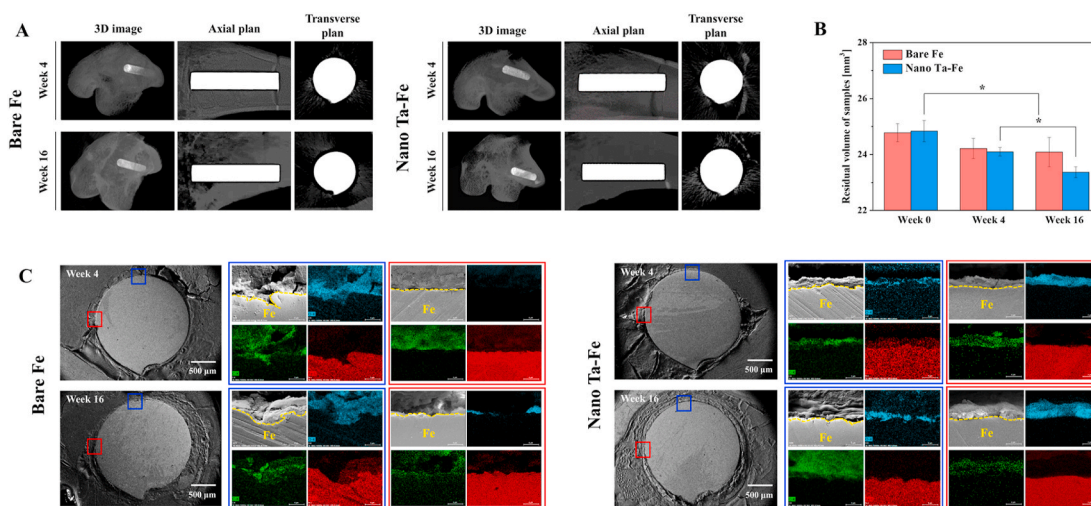
Fig. 6. (A) Three-dimensional (3D) reconstruction images of micro-computed tomography scans after 4 and 16 weeks of *in vivo* experiments. (B) Residual volume of bare Fe and nano Ta–Fe after 4 and 16 weeks. Statistical significance is indicated as * ($p < 0.05$). (C) Scanning electron microscopy images and corresponding energy-dispersive X-ray spectroscopy mapping images obtained from rectangular regions in the cross sections of bare Fe and nano Ta–Fe after 4 and 16 weeks of *in vivo* degradation testing (oxygen: light blue, iron: red, and carbon: green).
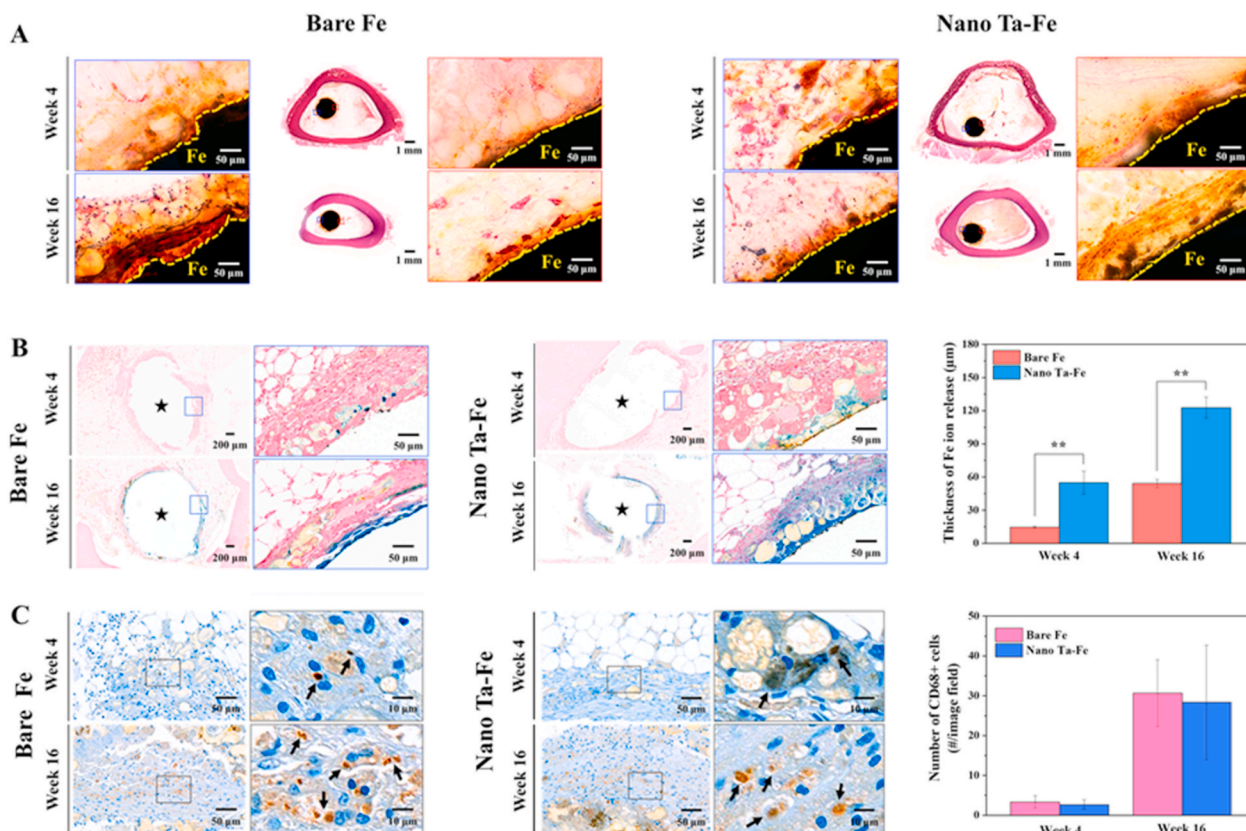

Fig. 7. *In vivo* histological and immunohistochemical characterization of the rabbit femur bone marrow implantation study. (A) Hematoxylin–eosin (H&E), (B) Prussian blue, and (C) CD68$^+$ stained mid-diaphyseal femoral cross sections. The average thickness of Fe ions released into the bone marrow tissue and the number of CD68$^+$ macrophages in the bone marrow of the rabbit are presented in (B) and (C), respectively, as a function of *in vivo* implantation time. Black stars in (B) indicate the implant inserted regions. Statistical significance is indicated as ** ($p < 0.005$).

ion penetration in the bone marrow tissue. Even in the low-magnification image, the Fe^{3+}-ion-penetrated regions were easily observable around the nano Ta–Fe sample and appeared to have a relatively uniform distribution with an average thickness of 131.0 ± 18.0 μm. Although bare Fe also exhibited a significant increase in the average ion penetration depth from 18.5 ± 13.7 μm to 113.1 ± 68.4 μm

from week 4–16 of implantation, there was marked inhomogeneity along the inner surface of the bone marrow tissue, and no blue-stained tissues were observed.

To investigate the immune responses, the expression of macrophages in the bone marrow tissue was detected by immunohistochemical staining for the CD68 marker, which is known to play a dominant role in

foreign body reaction, acute/chronic inflammation, and implant loosening [33]. As illustrated in Fig. 7(C), at week 4 of implantation, both bare Fe and nano Ta–Fe presented a small number of brown-stained CD68-positive macrophages in the bone marrow tissue, and their numbers significantly increased with increased implantation time up to 16 weeks. Although nano Ta–Fe exhibited slightly lower average macrophage numbers than bare Fe at weeks 4 and 16, there were no statistical differences between them ($p = 0.732$ at week 4 and $p = 0.909$ at week 16).

4. Discussion

Although Fe is known for its high potential as a biodegradable implant, a limitation to using this material for orthopedic injury is its extremely slow degradation rate [1,21]. In addition, in a physiological environment, deep and narrow local degradation zones forming on the surface of Fe may lead to significant deterioration of its mechanical performance, resulting in unexpected mechanical failure of the Fe implant before the bone healing process is completed [3,34]. In this study, to address this problem, we developed a novel combination of a nanostructured surface topography and galvanic reaction to achieve uniform and accelerated degradation of the Fe implant. As a nanostructured surface possesses an extremely large surface-area-to-volume ratio, this combination can substantially increase the contact surfaces between an Fe implant and corrosive body fluids, thereby effectively enhancing the degradation rate of the Fe implant. In addition, nanostructured surfaces have similar dimensions to those of the components of an extracellular matrix, which offers the unique ability to directly influence cellular and molecular events on the implant surface [25,26].

To develop nanostructured surface galvanic pairs on the Fe substrate, we employed the recently developed TIPS technique with Ta as a source of ion implantation as shown in Fig. 8. The TIPS technique enables the generation of numerous positive Ta ions from the Ta sputtering gun and their subsequent implantation on the negatively charged surface of the Fe substrate by applying the substrate bias [25,27]. As illustrated in the supplemental results (Fig. S7), the degree of the applied negative bias voltage to the Fe substrate determined the variation in surface roughness of the Fe substrate due to the influence of incident Ta ion energy and the surface erosion rate of the Fe substrate. By applying low negative substrate bias voltages ($\leq$500 V), incoming Ta ions had insufficient kinetic energy to sputter the Fe substrate, and dense and crack-free Ta coatings were formed on the surface of the Fe substrate. In contrast, with an applied bias voltage of −1000 V, Ta ions were strongly accelerated by the sheath electric field and impact on the top surface of the Fe substrate, resulting in continuous surface erosion of the Fe substrate rather than deposition [27]. More importantly, as illustrated in the cross-sectional STEM images of the surface (Fig. 1(e)), the Ta element was inhomogeneously implanted into the Fe surface, which was considered to be the cause of the local surface erosion rate differences, and thus, the development of surface nanostructures [35,36]. Due to this unique

characteristic of the TIPS technique, the nanostructured surface layer possessed excellent structural continuity and integrity with the Fe substrate without any visible physical interface. In addition, a considerable amount of Ta (<50 at%) was stably implanted in the upper region of the surface nanostructure, indicating that it should achieve mechanically robust Ta–Fe nano-galvanic pairs (Fig. 1(f)).

In terms of electrochemical activity, Ta has a lower reversible electrode potential and active position in the standard electrode potential series compared with Fe. However, because of the stable surface oxide layer of Ta, called a passive film, its corrosion potential is considerably shifted towards the positive direction, resulting in occupying the noble position in the galvanic pair with Fe [37–40]. As a result, when the nano Ta–Fe sample was in contact with aqueous environments, its nanostructured surface involved the formation of electrochemical nano-galvanic corrosion cells and became an excellent starting point for uniform surface degradation with no preferential sites. Because the dimension of surface features of nano Ta–Fe were in the nanometer range with well-defined surface pattern gaps, its effective surface area could greatly increase with good water absorbing ability of the nano Ta–Fe surface layer. These physical surface characteristics are known to affect the value of the charge transfer resistance and induce corrosion potential shift to more negative values. This was a key factor in the homogeneous decrease in the overall Fe surface potential (Fig. 2(a) and (b)) and uniform surface degradation behavior (Fig. 4(A) and (C)) of the nano Ta–Fe sample compared to that of bare Fe.

According to electrochemical and immersion tests (Fig. 2(c)–(d) and 3), bare Fe exhibited a relatively inactive surface compared to nano Ta–Fe, and most of the surface retained its initial flat and smooth surface morphology during the entire immersion period. This indicates the formation of close and intimate adhesion between the degradation product layer and the Fe substrate, thereby providing a stable physical barrier in enhancing corrosion resistance and reducing Fe surface degradation. In contrast, the nano Ta–Fe surface provided only a limited area (top of the surface nanostructures) at the interface. Under the degradation product, the surface nanostructures led to continuous access to the aqueous environment and long-lasting electrochemical activity [21].

In vitro mechanical and *in vivo* degradation assessments verified that the surface nano-galvanic corrosion cells of nano Ta–Fe enabled uniform surface degradation and consistent mechanical performance within 40 weeks. For bare Fe, with body fluid exposure, localized surface degradation of Fe was randomly initiated by the competitive adsorption between chloride ions and passive species (e.g., hydroxide ions and dipoles of water molecules) [34,41]. Once the concentration of chloride ions reached a critical value on the surface of the Fe substrate, it was possible to initiate and propagate the local Fe degradation over a long period of time, which in turn produced readily observable deep and irregular craters on the surface of the Fe substrate (Fig. 4(C) [*in vitro*] and 7 A [*in vivo*]). This behavior is regarded as one of the most destructive and insidious types of metal degradation, and directly affects not only the

Fig. 8. Schematic diagram of the TIPS process for Fe implants with Ta sputter target and negative substrate bias voltage of 1000 V.

strength, but also ductility of the implant [21–23].

The presence of surface irregularities can easily lead to stress concentration in the deep and narrow crater regions under physiological load conditions that may subsequently trigger the uncontrollable propagation of cracks at lower strain and stress levels than on a uniform surface [42,43]. Because the design, manufacturing, and assessment of orthopedic implants are generally based on the assumption of consistent mechanical performance after implantation, bare Fe can no longer be regarded as acceptable and safe for use in clinical practice. In contrast, for the nano Ta–Fe sample, numerous nano-galvanic cells formed on its surface were crucial to the enhancement of surface degradation activity and resulted in uniformly distributed degradation sites with a significant reduction in surface roughness both *in vitro* and *in vivo*. Therefore, despite its higher volumetric loss than that of the bare Fe sample, nano Ta–Fe exhibited almost unchanged values of the UTS and elongation rate up to 40 weeks of immersion. These long-term statistical results imply that the nano Ta–Fe implant can be regarded as a long-term reliable and stable treatment option in clinical practice.

Biocompatibility of the bare Fe and nano Ta–Fe samples was confirmed by both *in vitro* cellular response and *in vivo* animal tests. Although Fe participates in a wide variety of metabolic processes in the body, when the number of released Fe ions from the implant exceeds the tolerable limit for uptake by intracellular elements, cells inevitably suffer various degree of cytotoxicity, and severe immunogenic responses can be triggered, thus limiting the efficacy and biosafety of Fe [44,45]. In fact, as illustrated in Figs. 3(D) and 7(B), nano Ta–Fe exhibited an almost twofold higher level of Fe ion release than the bare Fe implant in the SBF immersion test, and after implantation into the rabbit femur medullary cavity, Fe ions were more broadly distributed in the bone marrow tissue around the nano Ta–Fe implant than bare Fe. Therefore, to address this concern, we performed two different sets of *in vitro* assays in which osteoblasts were cultured on either the sample surfaces directly with fresh culturing media (case 1) or culture plates with culturing media obtained after pre-incubation with bare Fe and nano Ta–Fe samples (case 2). The result of the case 1 assay revealed that nano Ta–Fe provided a favorable surface environment for cell attachment and spreading, exhibiting a higher number of adhered osteoblasts on its surface with a wider spreading morphology than on bare Fe (Fig. 5(B)). In addition, the osteoblasts proliferated almost threefold from day 1–3 with no difference in cell viability between the bare Fe and nano Ta–Fe samples at any culturing time point in the case 2 assay (Fig. 5(C)).

It has been demonstrated that extremely high concentrations of Fe ions (≥ 170 μg/ml) lead to oxidative damage to lipids, suppressed mitochondrial activity, and the formation of large precipitates in the cytoplasm, thereby inducing severe cell damage [44]. In this study, the accumulated Fe ion concentration up to 28 days for the bare Fe and nano Ta–Fe samples was only 22.4 μg/ml and 51.0 μg/ml, respectively, which was in the range of biologically acceptable tolerance in terms of metabolism. In addition, supplemental pH testing demonstrated that the bare Fe and nano Ta–Fe samples exhibited negligible pH increase during the 14 days of immersion in SBF solution (Fig. S8). The *in vitro* assay was well matched with the *in vivo* immunohistological analysis, in which the nano Ta–Fe implant did not exhibit any signs of local toxicity compared to the pure Fe implant (Fig. 7(C)). In addition, previous studies indicated that nanostructured surfaces, such as pores, wells, and grooves, are able to elicit biologically active cellular responses by regulating integrin-dependent cell adhesion signaling pathways [25,26,46–48]. In particular, surface features in the size range of 200–300 nm have demonstrated a profound effect on the surface hydrophilicity and formation of focal adhesion and filopodia extensions of cells, leading to a considerable extension of the cell structure compared to flat or micro-structured surfaces [25]. During this process, filopodia play an essential and primary role in signaling and sensing the surrounding microenvironment and stabilizing the cytoskeleton structure of cells on top of the surface nanostructures [26]. Therefore, the formation of numerous filopodia-like cell extrusions and enhanced cell spreading

behavior of osteoblasts on nano Ta–Fe indicated active cell surface interaction, thereby increasing the probability of forming intimate implant contact with the host bone tissue. The substantially improved surface hydrophilicity of nano Ta–Fe also led to high affinity for blood by preventing platelet adhesion and activation on its surface. Because hydrophobic surfaces lead to the strong adsorption and irreversible conformational change of blood proteins via hydrophobic interaction, the hydrophilic surface property of nano Ta–Fe prevented protein denaturation and suppressed subsequent platelet recruitment, adhesion, and activation (Fig. 5(D) and (E)) [24].

5. Conclusion

In this study, a novel strategy to accelerate the degradation rate of Fe implants with uniform surface degradation was demonstrated using the TIPS surface modification technique. With this technique, numerous Ta ions were generated and accelerated strongly toward the surface of the Fe implant by applying a high negative bias voltage to the Fe implant, which made it possible to develop Ta-implanted nanostructures on the Fe implant surface via continuous Fe surface erosion. Due to the higher corrosion potential of Ta than Fe, the surface of nano Ta–Fe acted as effective nano-galvanic couples under body fluid conditions and led to an increased rate of surface corrosion. Despite the relatively high degradation rate of nano Ta–Fe, its uniform surface degradation made it possible to exhibit consistent mechanical properties for up to 40 weeks of immersion. The *in vitro* osteoblast assay and *in vivo* rabbit femur medullary cavity implantation confirmed that nano Ta–Fe enhanced osteoblast adhesion and spreading on the surface. In addition, there was no sign of cellular or tissue toxicity despite the higher level of released Fe ions for nano Ta–Fe than the bare Fe implant. The present study thus demonstrates that the TIPS technique offers a new and safe approach in the pretreatment of Fe orthopedic implants to achieve an accelerated degradation rate and enhance the clinical outcome and biosafety of implants.

CRediT authorship contribution statement

Min-Kyu Lee: Conceptualization, Methodology, Validation, Investigation. **Hyun Lee:** Methodology, Validation, Investigation, Writing – original draft. **Cheonil Park:** Validation, Investigation. **In-Gu Kang:** Investigation. **Jinyoung Kim:** Validation. **Hyoun-Ee Kim:** Supervision, Project administration. **Hyun-Do Jung:** Conceptualization, Methodology, Writing – original draft, Writing – review & editing. **Tae-Sik Jang:** Conceptualization, Methodology, Writing – original draft, Writing – review & editing.

Declaration of competing interest

There are no conflicts of interest to declare.

Acknowledgment

Appendix A. Supplementary data

Supplementary data to this article can be found online at https://doi.org/10.1016/j.bioactmat.2021.07.003.

References

[1] H.N. Wang, Y. Zheng, Y. Li, C.B. Jiang, Improvement of in vitro corrosion and cytocompatibility of biodegradable Fe surface modified by Zn ion implantation, Appl. Surf. Sci. 403 (2017) 168–176.

[2] Y. Qi, X. Li, Y. He, D. Zhang, J. Ding, Mechanism of acceleration of iron corrosion by a polylactide coating, ACS Appl. Mater. Interfaces 11 (2019) 202–218.

[3] Y.F. Zheng, X.N. Gu, F. Witte, Biodegradable metals, Mater. Sci. Eng. R Rep. 77 (2014) 1–34.

[4] M.-H. Kang, K.-H. Cheon, K.-I. Jo, J.-H. Ahn, H.-E. Kim, H.-D. Jung, et al., An asymmetric surface coating strategy for improved corrosion resistance and vascular compatibility of magnesium alloy stents, Mater. Des. 196 (2020) 109182.

[5] H.F. Li, Y.F. Zheng, L. Qin, Progress of biodegradable metals, Prog Nat Sci-Mater. 24 (2014) 414–422.

[6] Y.J. Chen, Z.G. Xu, C. Smith, J. Sankar, Recent advances on the development of magnesium alloys for biodegradable implants, Acta Biomater. 10 (2014) 4561–4573.

[7] D.H. Zhu, I. Cockerill, Y.C. Su, Z.X. Zhang, J.Y. Fu, K.W. Lee, et al., Mechanical strength, biodegradation, and in vitro and in vivo biocompatibility of Zn biomaterials, ACS Appl. Mater. Interfaces 11 (2019) 6809–6819.

[8] Z.Z. Yin, W.C. Qi, R.C. Zeng, X.B. Chen, C.D. Gu, S.K. Guan, et al., Advances in coatings on biodegradable magnesium alloys, J Magnes Alloy 8 (2020) 42–65.

[9] K.-H. Cheon, C. Park, M.-H Kang, M.-K Lee, H. Lee, H.-E Kim, H.-D Jung, T.-S Jang, Construction of tantalum/poly (ether imide) coatings on magnesium implants with both corrosion protection and osseointegration properties, Bioact. Mater. 6 (4) (2021) 1189–1200.

[10] X. Tong, Z.M. Shi, L.C. Xu, J.X. Lin, D.C. Zhang, K. Wang, et al., Degradation behavior, cytotoxicity, hemolysis, and antibacterial properties of electro-deposited Zn-Cu metal foams as potential biodegradable bone implants, Acta Biomater. 102 (2020) 481–492.

[11] Y. Liu, Y. Zheng, X.-H. Chen, J.-A. Yang, H. Pan, D. Chen, et al., Fundamental theory of biodegradable metals—definition, criteria, and design, Adv. Funct. Mater. 29 (2019) 1805402.

[12] K.-H. Cheon, C. Park, M.-H. Kang, I.-G. Kang, M.-K. Lee, H. Lee, et al., Construction of tantalum/poly (ether imide) coatings on magnesium implants with both corrosion protection and osseointegration properties, Bioactive materials 6 (2021) 1189–1200.

[13] J. Zhang, H.S. Shi, J.Q. Liu, T. Yu, Z.H. Shen, J.D. Ye, Good hydration and cell-biological performances of superparamagnetic calcium phosphate cement with concentration-dependent osteogenesis and angiogenesis induced by ferric iron, J. Mater. Chem. B 3 (2015) 8782–8795.

[14] W. Lin, H. Zhang, W. Zhang, H. Qi, G. Zhang, J. Qian, et al., In vivo degradation and endothelialization of an iron bioresorbable scaffold, Bioactive materials 6 (2020) 1028–1039.

[15] Y.L. Liao, H.B. Cao, B. Xia, Q.Y. Xiao, P. Liu, G.L. Hu, et al., Changes in trace element contents and morphology in bones of duck exposed to molybdenum or/ and cadmium, Biol. Trace Elem. Res. 175 (2017) 449–457.

[16] M. Peuster, P. Wohlsein, M. Brügmann, M. Ehlerding, K. Seidler, C. Fink, et al., A novel approach to temporary stenting: degradable cardiovascular stents produced from corrodible metal—results 6–18 months after implantation into New Zealand white rabbits, Heart 86 (2001) 563–569.

[17] T. Kraus, F. Moszner, S. Fischerauer, M. Fiedler, E. Martinelli, J. Eichler, et al., Biodegradable Fe-based alloys for use in osteosynthesis: outcome of an in vivo study after 52weeks, Acta Biomater. 10 (2014) 3346–3353.

[18] W. Lin, L. Qin, H. Qi, D. Zhang, G. Zhang, R. Gao, et al., Long-term in vivo corrosion behavior, biocompatibility and bioresorption mechanism of a bioresorbable nitrided iron scaffold, Acta Biomater. 54 (2017) 454–468.

[19] R. Waksman, R. Pakala, R. Baffour, R. Seabron, D. Hellinga, F.O. Tio, Short-term effects of biocorrodible iron stents in porcine coronary arteries, J. Intervent. Cardiol. 21 (2008) 15–20.

[20] M. Peuster, C. Hesse, T. Schloo, C. Fink, P. Beerbaum, C. von Schnakenburg, Long-term biocompatibility of a corrodible peripheral iron stent in the porcine descending aorta, Biomaterials 27 (2006) 4955–4962.

[21] J. Zhou, Y. Yang, M. Alonso Frank, R. Detsch, A.R. Boccaccini, S. Virtanen, Accelerated degradation behavior and cytocompatibility of pure iron treated with sandblasting, ACS Appl. Mater. Interfaces 8 (2016) 26482–26492.

[22] J. Cheng, T. Huang, Y.F. Zheng, Relatively uniform and accelerated degradation of pure iron coated with micro-patterned Au disc arrays, Mater Sci Eng C Mater Biol Appl 48 (2015) 679–687.

[23] T. Huang, Y. Zheng, Uniform and accelerated degradation of pure iron patterned by Pt disc arrays, Sci. Rep. 6 (2016) 23627.

[24] C. Park, S.-W. Lee, J. Kim, E.-H. Song, H.-D. Jung, J.-U. Park, et al., Reduced fibrous capsule formation at nano-engineered silicone surfaces via tantalum ion implantation, Biomater Sci 7 (2019) 2907–2919.

[25] C. Park, Y.-J. Seong, I.-G. Kang, E.-H. Song, H. Lee, J. Kim, et al., Enhanced osseointegration ability of poly(lactic acid) via tantalum sputtering-based plasma immersion ion implantation, ACS Appl. Mater. Interfaces 11 (2019) 10492–10504.

[26] B.S. Moon, S. Kim, H.E. Kim, T.S. Jang, Hierarchical micro-nano structured Ti6Al4V surface topography via two-step etching process for enhanced hydrophilicity and osteoblastic responses, Mater Sci Eng C Mater Biol Appl 73 (2017) 90–98.

[27] T.-S. Jang, S. Kim, H.-D. Jung, J.-W. Chung, H.-E. Kim, Y.-H. Koh, et al., Large-scale nanopatterning of metal surfaces by target-ion induced plasma sputtering (TIPS), RSC Adv. 6 (2016) 23702–23708.

[28] T. Lu, J. Wen, S. Qian, H. Cao, C. Ning, X. Pan, et al., Enhanced osteointegration on tantalum-implanted polyetheretherketone surface with bone-like elastic modulus, Biomaterials 51 (2015) 173–183.

[29] C. Yang, J. Li, C. Zhu, Q. Zhang, J. Yu, J. Wang, et al., Advanced antibacterial activity of biocompatible tantalum nanofilm via enhanced local innate immunity, Acta Biomater. 89 (2019) 403–418.

[30] B. Liu, Y.F. Zheng, Effects of alloying elements (Mn, Co, Al, W, Sn, B, C and S) on biodegradability and in vitro biocompatibility of pure iron, Acta Biomater. 7 (2011) 1407–1420.

[31] A.F. Cipriano, J. Lin, A. Lin, A. Sallee, B. Le, M.C. Cortez Alcaraz, et al., Degradation of bioresorbable Mg–4Zn–1Sr intramedullary pins and associated biological responses in vitro and in vivo, ACS Appl. Mater. Interfaces 9 (2017) 44332–44355.

[32] F. Witte, J. Fischer, J. Nellesen, H.-A. Crostack, V. Kaese, A. Pisch, et al., In vitro and in vivo corrosion measurements of magnesium alloys, Biomaterials 27 (2006) 1013–1018.

[33] J.C. Doloff, O. Veiseh, A.J. Vegas, H.H. Tam, S. Farah, M. Ma, et al., Colony stimulating factor-1 receptor is a central component of the foreign body response to biomaterial implants in rodents and non-human primates, Nat. Mater. 16 (2017) 671–680.

[34] H. Amar, J. Benzakour, A. Derja, D. Villemin, B. Moreau, A corrosion inhibition study of iron by phosphonic acids in sodium chloride solution, J. Electroanal. Chem. 558 (2003) 131–139.

[35] I.P. Jain, G. Agarwal, Ion beam induced surface and interface engineering, Surf. Sci. Rep. 66 (2011) 77–172.

[36] X. Li, Y. An, Y. Wei, H. Du, L. Hou, C. Guo, et al., Influence of surface nanocrystallization on Ti ion implantation of pure iron, J. Mater. Sci. Technol. 31 (2015) 305–310.

[37] W. Jin, G. Wang, Z. Lin, H. Feng, W. Li, X. Peng, et al., Corrosion resistance and cytocompatibility of tantalum-surface-functionalized biomedical ZK60 Mg alloy, Corrosion Sci. 114 (2017) 45–56.

[38] M.D. Anderson, B. Aitchison, D.C. Johnson, Corrosion resistance of atomic layer deposition-generated amorphous thin films, ACS Appl. Mater. Interfaces 8 (2016) 30644–30648.

[39] C.-Y. Li, C. Yu, R.-C. Zeng, B.-C. Zhang, L.-Y. Cui, J. Wan, et al., In vitro corrosion resistance of a Ta2O5 nanofilm on MAO coated magnesium alloy AZ31 by atomic layer deposition, Bioactive Materials 5 (2020) 34–43.

[40] R.W. Revie, Uhlig's Corrosion Handbook, John Wiley & Sons, 2011.

[41] M. Schinhammer, P. Steiger, F. Moszner, J.F. Löffler, P.J. Uggowitzer, Degradation performance of biodegradable FeMnC(Pd) alloys, Mater. Sci. Eng. C 33 (2013) 1882–1893.

[42] K.H. Cheon, C. Gao, M.H. Kang, H.D. Jung, T.S. Jang, H.E. Kim, et al., A crack-free anti-corrosive coating strategy for magnesium implants under deformation, Corrosion Sci. 132 (2018) 116–124.

[43] D. Bian, W. Zhou, Y. Liu, N. Li, Y. Zheng, Z. Sun, Fatigue behaviors of HP-Mg, Mg-Ca and Mg-Zn-Ca biodegradable metals in air and simulated body fluid, Acta Biomater. 41 (2016) 351–360.

[44] S. Zhu, N. Huang, L. Xu, Y. Zhang, H. Liu, H. Sun, et al., Biocompatibility of pure iron: in vitro assessment of degradation kinetics and cytotoxicity on endothelial cells, Mater. Sci. Eng. C 29 (2009) 1589–1592.

[45] N.S. Fagali, C.A. Grillo, S. Puntarulo, M.A.F.L. de Mele, Cytotoxicity of corrosion products of degradable Fe-based stents: relevance of pH and insoluble products, Colloids Surf., B 128 (2015) 480–488.

[46] Q. Liu, S. Zheng, K. Ye, J. He, Y. Shen, S. Cui, et al., Cell migration regulated by RGD nanospacing and enhanced under moderate cell adhesion on biomaterials, Biomaterials 263 (2020) 120327.

[47] T.-S. Jang, J.H. Lee, S. Kim, C. Park, J. Song, H.J. Jae, H.-E. Kim, J.W. Chung, H.-D Jung, et al., Ta ion implanted nanoridge-platform for enhanced vascular responses, Biomaterials 223 (2019) 119461.

[48] M.-K Lee, H. Lee, H.-E. Kim, E.-J. Lee, T.-S. Jang, H.-D. Jung, Nano-topographical control of Ti-Nb-Zr alloy surfaces for enhanced osteoblastic response, Nanomaterials 11 (6) (2021) 1507.